



Mo promoting Ni-based catalysts confined by halloysite nanotubes for dry reforming of methane: Insight of coking and H₂S poisoning resistance

Jiajia Zheng^a, Sarawoot Impeng^b, Jun Liu^a, Jiang Deng^{a,*}, Dongsong Zhang^{a,*}

^a International Joint Laboratory of Catalytic Chemistry, State Key Laboratory of Advanced Special Steel, Department of Chemistry, Research Center of Nano Science and Technology, College of Sciences, Shanghai University, Shanghai 200444, China

^b National Nanotechnology Center, National Science and Technology Development Agency, Pathum Thani 12120, Thailand

ARTICLE INFO

Keywords:

Dry reforming of methane
Ni-based catalysts
Coking resistance
H₂S poisoning

ABSTRACT

Dry reforming of methane (DRM) shows promise for converting greenhouse gases into syngas but developing stable Ni-based catalysts resistant to sintering, coking, and H₂S poisoning is challenging. We developed a highly effective catalyst by confining Mo-promoted Ni-based catalysts within halloysite nanotubes. Mo alloying with Ni inhibits Ni particles' migration out of the nanotubes, preventing the sintering of metals while decreasing the graphitic degree of carbon, which can balance the formation and removal of coke. Mo slows down H₂S poisoning on Ni by adsorbing it competitively, maintaining a balance between carbon formation and removal even when H₂S adsorbed on Mo hinders its role. With the inclusion of Mo, the rate of deactivation in the presence of H₂S was reduced by half. Our research highlights the numerous advantages of Mo species and draws a correlation between carbon deposition and H₂S poisoning, which offer new insights for designing efficient DRM catalysts.

1. Introduction

The increase in greenhouse gas emissions leads to severe global warming. As two primary greenhouse gases, utilizing CH₄ and CO₂ comprehensively and efficiently is significant for mitigating climate warming [1,2]. Dry reforming of methane (DRM) can convert these greenhouse gases into syngas (CO, H₂) with a ratio of 1:1, which can be used in Fischer-Tropsch synthesis to produce high value-added chemicals to realize effective conversion and utilization of resources while reducing greenhouse gas emissions [3,4]. Ni-based catalysts are widely used in DRM reactions due to the low cost and catalytic performance comparable to that of precious metals. However, Ni-based catalysts are susceptible to the sintering of active components and coke deposition in high-temperature reactions, which lead to the deactivation of catalysts [5–7]. In addition, biogas contains certain H₂S impurities. It has strong chemisorption on metal surfaces, especially for Ni, which can cause active metal poisoning and seriously affect the catalytic performance [8–11]. Therefore, it is essential to design an efficient and stable Ni-based catalyst with resistance to sintering, carbon deposition, and H₂S poisoning for DRM.

There are many reports on improving the sintering and coking resistance of Ni-based catalysts, such as enhancing metal-support

interaction, structural confinement and adding additives, etc. Generally, strong metal-support interaction (SMSI) is known to help inhibit metal sintering, and manufacturing defect sites and spinel exsolution are effective ways to enhance the SMSI, facilitating the anchoring of Ni [12–14]. In addition, small-size Ni nanoparticles (NPs) are certified to effectively inhibit sintering and coking [15,16]. Moreover, researchers studied the confinement effect derived from the steric hindrance effect, which would hinder particle migration and growth [17]. For example, a hollow pure silicon molecular sieve or mesoporous silica can be used to fabricate Ni NPs with high dispersion and uniform size [18]. The steric confinement effect significantly controls the size of metal particles and inhibits the sintering and coking of particles. Furthermore, alloying Ni with other high melting point metals would contribute to improve the dispersion of metal NPs and sintering resistance of catalysts. Simultaneously, alloying can regulate the electronic state of the active metal to promote the activity of catalysts [19–23]. Consequently, the combination of steric confinement and alloying strategy would be promising for the fabrication of Ni-based catalysts with coking and sintering resistance.

Generally, the impurity of H₂S depend on the resource of CH₄. For example, the H₂S in biogas produced by anaerobic digestion of organic matter is 0–3% [11]. Currently, relatively little attention has been paid

* Corresponding authors.

E-mail addresses: jiangdeng@shu.edu.cn (J. Deng), dszhang@shu.edu.cn (D. Zhang).

<https://doi.org/10.1016/j.apcatb.2023.123369>

Received 3 July 2023; Received in revised form 29 September 2023; Accepted 6 October 2023

Available online 7 October 2023

0926-3373/© 2023 Elsevier B.V. All rights reserved.

to the H₂S poisoning effect of Ni-based catalysts in DRM reactions. Some typical anti-poisoning methods in the existing research include oxidizing sulfide [24,25], adding metal additives [8,26], and creating sacrifice sites [27–29] etc. For instance, Theofanidis et al. studied the effect of Rh in Ni-based catalysts on H₂S impurities during steam-dry reforming, showing that Ni-Rh surface alloys inhibited the dissociation of H₂S [8]. Moreover, the core-shell structure where the outer layer served as the protected layer was designed to improve the H₂S tolerance of Ni-based catalysts [24]. In addition, according to Liu et al. [27], Mo species can enhance the resistance to H₂S poisoning by competing with it for adsorption. This, in turn, helps to prevent the deactivation of SiO₂-supported Ni catalysts. Nevertheless, it remains unclear how the combined impact of H₂S poisoning, coking, and metal sintering affect Ni-based catalysts for DRM.

Halloysite nanotubes (Al₂Si₂O₅(OH)₄·nH₂O, HNTs) are natural, tubular aluminosilicate clay minerals possessing good thermal stability and unique hollow tubular structure, which can be used as ideal natural nanocarrier [30,31]. Abundant surface groups of HNTs with an internal alumina layer (Al-OH) and an external silicate layer (Si-O-Si) are good active sites for anchoring oxides and allow a wide variety of chemical modifications [32–34]. Recently, the high melting point transition metal Mo species have been shown to be effective in eliminating carbon deposition in DRM, and the catalytic effect is superior when the molar ratio of Ni-Mo is between 4 and 5 [35–37]. In addition, the Mo component is widely used in various desulfurization processes due to its excellent absorption and resistance to sulfur components [38,39]. However, the simultaneous application of Mo to inhibit carbon deposition and resist H₂S poisoning in DRM has not been reported. Herein, we fabricated Mo modified Ni-based catalysts confined in HNTs (NiMo/A-H), which improved coking resistance and alleviate H₂S poisoning of catalysts. The effect between H₂S poisoning and carbon deposition was revealed through in situ Raman characterization. Compared with other Ni-based catalysts focused on resisting sulfur poisoning, NiMo/A-H catalyst possesses good resistance to sintering and carbon deposition, as well as sulfur tolerance, which is a comprehensive catalyst with multiple resistance. This provides a new idea for designing efficient DRM catalysts with carbon deposition resistance and H₂S resistance.

2. Experiments

2.1. Preparation of catalysts

2.1.1. Pretreatment of Halloysite Nanotubes

The HNTs were treated with acid to selectively etch alumina inside the HNTs tubes in a process like that described by Garcia-Garcia et al. [40]. 2 g HNTs were added to 200 mL acetic acid solution with a concentration of 1.0 M and stirred on a heating plate at 50 °C for 72 h. Afterwards, the HNTs that were chemically modified underwent centrifugation and were rinsed using deionized water until the pH level reached between 6 and 7. Finally, acid-treated HNTs were dried overnight in an oven at 80 °C and were denoted as A-H.

2.1.2. Synthesis of Catalysts

Catalysts were synthesized by wet impregnation method. Firstly, Ni (NO₃)₂·6 H₂O, (NH₄)₆Mo₇O₂₄·6 H₂O, and A-H were mixed in deionized water, dissolved by ultrasound for 20 min, and then stirred at 40 °C for 3 h. After stirring vigorously, the mixture was dried by rotary evaporation and then dried in an oven at 80 °C for 24 h. The solids were obtained by calcination at 550 °C for 6 h in a muffle furnace. The Ni/Mo molar ratio of synthesized catalyst is 4:1, and the catalyst was denoted as NiMo/A-H. Catalysts with different Ni/Mo ratios were denoted as Ni₃Mo₁, Ni₄Mo₁ (NiMo/A-H) and Ni₅Mo₁, respectively.

As comparison, Ni/A-H catalysts were prepared through the same method as above without molybdate species. Ni/H catalysts were fabricated by using the untreated HNTs as the support. The Ni content

for all catalysts was controlled at 5 wt%.

2.2. Catalysts characterization

2.2.1. In situ study

The 20 mg sample was placed into the ceramic tube in the Linkam reactor. Raman experiments were performed using a 325 nm laser on the LabRAM HR Evolution. The spectra were acquired in the 100–2000 cm⁻¹ range with 0.65 cm⁻¹ of spectral resolution. In situ spectra over Ni/A-H and NiMo/A-H catalysts were carried out in a flow of CH₄/CO₂/N₂ (H₂S) (10/10/10 mL/min) at 800 °C after pretreated under N₂ at 300 °C for 30 min. Test conditions: Acq. time: 6 s, Accumulation: 2, Objective: x15_NUV, Grating: 1800, Total data points: 9.

2.2.2. Catalyst test

All catalysts were reduced in 10% H₂/N₂ at 750 °C for 1 h before the DRM reaction. The activity and stability of the catalysts (0.12 g sample diluted by 0.8 g 20–40 mesh quartz) were carried out in a quartz fixed-bed tubular reactor with a total gas flow rate of 140 mL/min (CH₄/CO₂ = 1:1, GHSV = 70,000 mL·g⁻¹·h⁻¹). The catalytic activity was successively increased by increasing the reaction temperature from 600 °C to 800 °C. The stability was performed at 800 °C for 50 h. An online gas chromatograph equipped with TCD was used to analyze the products.

H₂S resistance test of the catalysts was tested at 800 °C with the reactant gas stream CH₄/CO₂/H₂S = 1:1:0.17 (3.2 ppm H₂S balanced with N₂), GHSV = 62,000 mL·g⁻¹·h⁻¹. The DRM process was conducted for half an hour without the presence of H₂S, and then H₂S was flowed for three hours. Then, H₂S was switched into N₂, and the catalyst activity recovery over time was recorded.

The conversion of CH₄ and CO₂ was calculated as follows:

$$X_{\text{CH}_4}(\%) = \frac{[\text{CH}_4]_{\text{in}} - [\text{CH}_4]_{\text{out}}}{[\text{CH}_4]_{\text{in}}} \times 100$$

$$X_{\text{CO}_2}(\%) = \frac{[\text{CO}_2]_{\text{in}} - [\text{CO}_2]_{\text{out}}}{[\text{CO}_2]_{\text{in}}} \times 100$$

Where [CH₄] and [CO₂] represent the peak area of the inlet and outlet measured by TCD.

The H₂/CO ratio of product was determined by:

$$\frac{\text{H}_2}{\text{CO}} = \frac{\text{H}_2\text{produced}(\text{mol})}{\text{COproduced}(\text{mol})}$$

Turnover frequencies (s⁻¹) were calculated from the following:

$$\text{TOF}_{\text{CH}_4} = \frac{n[\text{CH}_4]}{\text{Weight of catalyst} \times w_{\text{Ni}}/58.69 \times \text{Dispersion} \times 60}$$

$$\text{TOF}_{\text{CO}_2} = \frac{n[\text{CO}_2]}{\text{Weight of catalyst} \times w_{\text{Ni}}/58.69 \times \text{Dispersion} \times 60}$$

where w_{Ni} is the weight percent of Ni over catalyst, and metal dispersion was determined by CO chemisorption experiments. n represents the molar conversion rate of CH₄ and CO₂.

2.2.3. Computational details

To gain insights into the poison-resistance of NiMo alloy catalysts towards H₂S, we conducted density functional theory (DFT) calculations to investigate the adsorption of H₂S on both Ni and NiMo catalysts. The computational methodology used in this study follows the procedure reported in our previous work. In brief, periodic DFT calculations were performed using the Vienna ab initio simulation package (VASP) [41]. The interactions between electrons and nuclei were described using projector-augmented wave pseudopotentials [42]. The exchange-correlation effects of electrons were treated using the generalized gradient approximation (GGA) with the Perdew-Burke-Ernzerhof (PBE) functional [43]. The energy cutoff of 400 eV was chosen for all

calculations. To explain van der Waals interactions, we incorporated the DFT-D3 method proposed by Grimme et al. [44]. The Brillouin zone was sampled using a $3 \times 3 \times 1$ k-point mesh for all calculations [45]. Specifically, we constructed Ni and NiMo (111) surfaces with dimensions of 4×4 and 2×2 , respectively.

The adsorption energy of H_2S on Ni and NiMo (111) surfaces was determined using the following equation: $E_{\text{ads}} = E_{\text{H}_2\text{S}/\text{surface}} - (E_{\text{H}_2\text{S}} + E_{\text{surface}})$.

In this equation, $E_{\text{H}_2\text{S}/\text{surface}}$ represents the total energy of the H_2S /surface complex, whereas $E_{\text{H}_2\text{S}}$ and E_{surface} correspond to the total energies of the isolated H_2S molecule and the pristine surface, respectively. According to this equation, a more negative value of the adsorption energy indicates a stronger adsorption of H_2S on the surface.

3. Results and discussion

3.1. Characterization of fresh catalysts

The NiMo/A-H catalyst was obtained by co-impregnating metal precursors over acid-treated HNTs (A-H), followed by hydrogen reduction after the calcination process. The synthesis procedure of NiMo/A-H is shown in Fig. 1. HNTs were first treated with acetic acid, which can selectively etch alumina in the inner layer of HNTs [40]. Elemental content analysis of the untreated and acid-treated HNTs (Table S1) shows that the Si/Al ratio of A-H is higher than that of HNTs, indicating that the Al content of the support is reduced after acid treatment, which confirms the etching of alumina. Acid etching enlarges the inner diameter of HNTs from 12.9 nm to 17.9 nm while the original nanotube-like morphology is still maintained (Fig. S1). As a result, the slight increase in the lumen facilitates the introduction of metal precursors. Moreover, the inner surface of HNTs is hydroxylated after acid-etching (Fig. S2a), which is favorable for the adsorption of metal precursors. The chemical environments of Si and Al in HNTs and A-H were studied by solid-state NMR spectra (Fig. S2b, c), and no significant change has been observed due to the slight etching. The specific surface area (SSA) and pore volume of the support show an increase after acid treatment (Table S2 and Fig. S3), indicating the enlarged diameter of HNTs. After the introduction of metals, the SSA of all catalysts decreases, and the NiMo/A-H catalyst owns the smallest SSA which might be ascribed to the occupation of metal NPs in the lumen.

The location of metal particles can be seen from the SEM diagram (Fig. S4). When compared to Ni/H catalyst, of which most nanoparticles are dispersed on the HNT surface, Ni/A-H and NiMo/A-H have few particles visible on their outer surface. Particularly, the metal particles inside the lumen are observed in Ni/A-H and NiMo/A-H (Fig. S5). Furthermore, as displayed in transmission electron microscopy (TEM) images, Ni NPs with average size of 19.7 nm is distributed outside the original HNTs, while Ni NPs with mean size of 14.7 nm have been distributed inside A-H (Fig. S6). It demonstrates that acid treatment plays a crucial role in endowing the metal NPs to locate into the inner of

nanotubes. Meanwhile, the size of the Ni NPs loaded inside the inner of HNT is controlled, confirming the importance of the confined structure. In addition, the introduction of Mo can lead to a reduction in particle size as alloys are formed (Fig. S6c), resulting in an average size of 10.1 nm. The entry of particles into the lumen of HNTs has been confirmed based on HRTEM images (Fig. 2). The lattice fringes spacing is observed at 0.205 nm, corresponding to the (111) crystal plane of Ni^0 (Fig. 2b). The energy dispersive spectroscopy (EDS) analyses were used to confirm the distribution of elements in the catalysts (Fig. 2c-i), proving that the elements Ni and Mo are preferably distributed in the tube. Furthermore, the HRTEM images of the sample show lattice fringe with a lattice distance of 0.199 nm, which corresponds to the (220) plane of Ni_4Mo (Fig. S7), confirming the formation of the alloy. Noticeably, line scanning profiles further confirm that Ni and Mo co-existed in the nanoparticles in a ratio of nearly 4:1. The results of argon-ion etched XPS (Fig. S8) show that the signal intensity of Ni^0 increases with the increase of etching time, which also supports the confined structure. The above results indicate that acid treatment promotes the entry of metal particles into the lumen of HNTs, and alloying further reduces the metal particle size.

X-ray diffraction (XRD) analysis of reduced catalysts was performed to characterize the crystalline structure of catalysts, as depicted in Fig. 3. The raw HNTs show typical peaks for HNTs species (20.1° , 24.7° , 35.0° , 38.4° , 54.6° and 62.5°), indexed to JCPDS#29-1487 ($\text{Al}_2\text{Si}_2\text{O}_5(\text{OH})_4$). In addition, it contains some impurity peaks of quartz (22.0° , 26.6°). As observed, chemically-etched HNTs exhibit XRD patterns comparable to untreated HNTs, indicating the preservation of the crystal structure after undergoing acid treatments [40]. After the thermal treatment, the reflections of HNTs are obviously weakened due to dehydroxylation and the formation of amorphous metahallosite [34]. The Ni/H catalyst shows intense peaks at 44.5° , 51.8° , and 76.4° , which can be assigned to (111), (200), and (220) planes of Ni^0 , respectively. For NiMo/A-H catalyst, no characteristic diffraction peak of Mo species is observed because of its low content. Meanwhile, local magnification of the XRD pattern shows that the Ni (111) peak shifts to a lower angle, which may be due to the slight expansion of the Ni lattice caused by the entry of Mo, indicating the formation of NiMo alloy [35].

The catalyst reducibility and metal-support interaction were evaluated by temperature-programmed reduction in hydrogen (H_2 -TPR), as shown in Fig. 4a. Typically, the high reduction peak temperature corresponds to the strong interaction between metal and support [46]. For Ni/H and Ni/A-H catalysts, the reduction peaks at low temperatures are attributed to the reduction of bulk NiO_x species located on the sample surface. This part of the NiO_x species has a large particle size and weak interaction with the support, so it is easy to be reduced. The peaks of 408°C and 430°C can be attributed to the reduction of NiO_x in the HNTs lumen or with relatively small particle size, indicating a stronger interaction with support. Additionally, the peak reduction temperature of Ni/A-H is higher than that of Ni/H, which indicates that acid treatment can enhance the interaction between metal and support. As for the

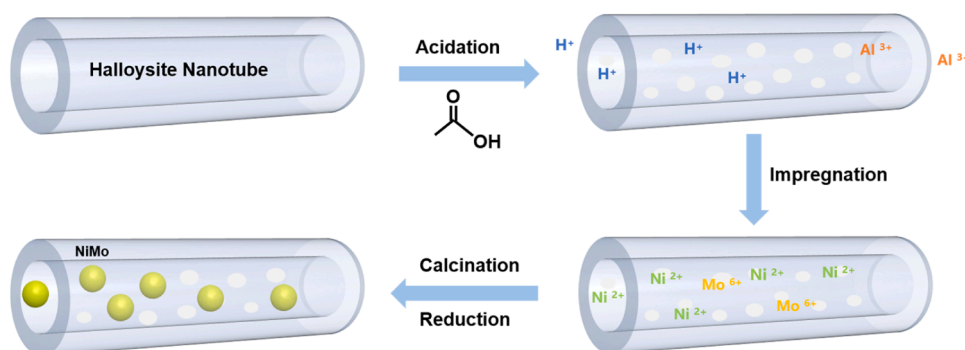


Fig. 1. Schematic illustration of the preparation of NiMo/A-H catalyst.

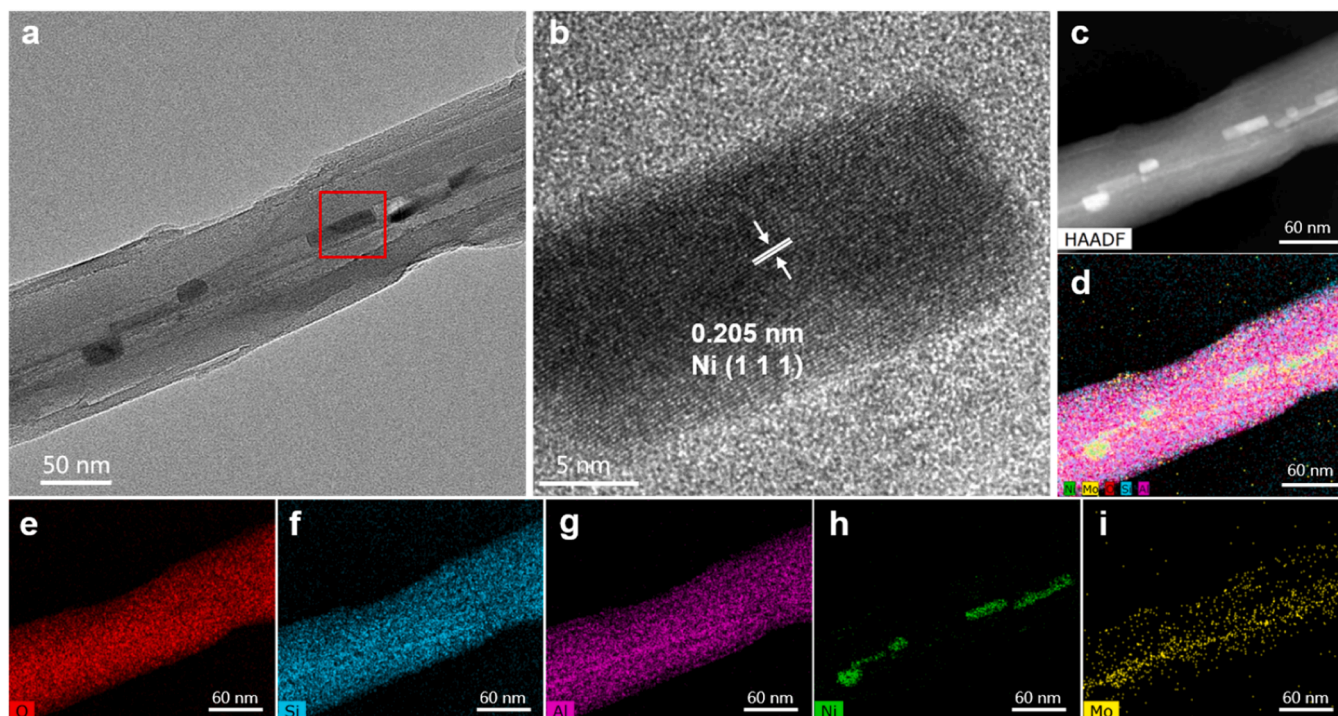


Fig. 2. (a) (b) HRTEM images, (c) HAADF-STEM image, (d-i) elemental mapping of NiMo/A-H catalyst.

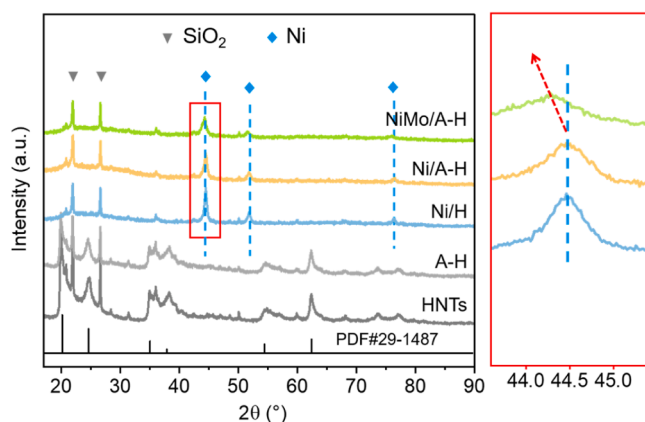


Fig. 3. XRD patterns of reduced catalysts.

NiMo/A-H catalyst, the peaks at lower temperatures can also be assigned to the reduction of larger NiO particles on the surface. The peaks of NiMo/A-H catalysts at 451 °C and 496 °C can be attributed to the reduction of NiO and MoO_x, further demonstrating the formation of NiMo alloys during reduction. It is obvious that all reduction peaks of the NiMo/A-H catalyst shift to higher temperatures, which indicates that NiO is more difficult to be reduced due to the stronger metal-support interaction of the catalyst. Moreover, the addition of Mo species increases H₂ consumption (Table 1), which means that MoO_x can also be reduced by H₂ to produce NiMo alloys. The results of H₂-TPR show that acid-treated support and the introduction of Mo species can enhance the metal-support interaction.

Surface electronic states of Ni for reduced catalysts were explored by X-ray photoelectron spectroscopy (XPS). As is shown in Fig. 4b, the peak in the spectrum at 852.4–852.9 eV is attributed to metallic Ni⁰ [47]. Peaks appearing at 854 eV and 857 eV are assigned to Ni²⁺ species in NiO and Ni(OH)₂, respectively [48]. Compared to the Ni/H catalyst, the Ni⁰ peak in Ni/A-H shifts to high binding energy, indicating that an

electronic interaction exists between the Ni and acid-treated support. Thus, the interaction between the metal and the support can be enhanced, which is in conformity to H₂-TPR results. Importantly, the peak of Ni⁰ in NiMo/A-H migrates towards the higher binding energy region, which indicates that a stronger charge transfer happens between Mo and Ni. Furthermore, 41.9% of Ni⁰ exists in NiMo/A-H, which is significantly higher than that in Ni/H and Ni/A-H catalysts, indicating that the introduction of Mo is beneficial to restrain the oxidation of Ni. Thus, the NiMo/A-H catalyst can possess more active sites to achieve superior catalytic performance. Additionally, the binding energy of Al 2p and Si 2p of catalysts (Fig. S9) does not change significantly, indicating that the chemical environment of Al and Si remains constant after acid-etching and Mo incorporation.

3.2. Surface properties of catalysts

To get insight into the ability of catalysts for the CH₄ activation, a temperature-programmed surface reaction (CH₄-TPSR) was performed, and the tail gas was linked to online mass spectrometry (MS) to monitor the desorption products. As shown in Fig. 5, all catalysts have peaks of CO₂ and H₂O between 300 and 400 °C and then quickly reach the maximum. The emergence of H₂O, CO, and CO₂ in the off-gas indicates the presence of residual O species (O_{ads}) on the surface of Ni NPs, which facilitates the decomposition of the CH₄, but these O species are rapidly consumed. The H₂ signal in the mass spectrum comes from the cleavage of CH₄ and is synchronized with the TCD signal. The initial temperatures of CH₄-consumption and H₂-generation peak for Ni/A-H (422 °C) and NiMo/A-H (415 °C) start at a lower temperature, as compared to 465 °C for Ni/H, whereas the peak positions of three catalysts are located at approximately 670 °C. The lower CH₄ pyrolysis temperature, larger CH₄ consumption and H₂ production of the NiMo/A-H catalyst indicate that it has a stronger activation ability for CH₄.

The adsorption and activation capability of catalysts for CO₂ was further investigated by temperature-programmed desorption of CO₂ coupling mass spectrum (CO₂-TPD-MS), as shown in Fig. S10. Compared to the Ni/H catalyst, Ni/A-H exhibits stronger adsorption of CO₂ with a large desorption peak. Meanwhile, obvious CO signals appear over Ni/

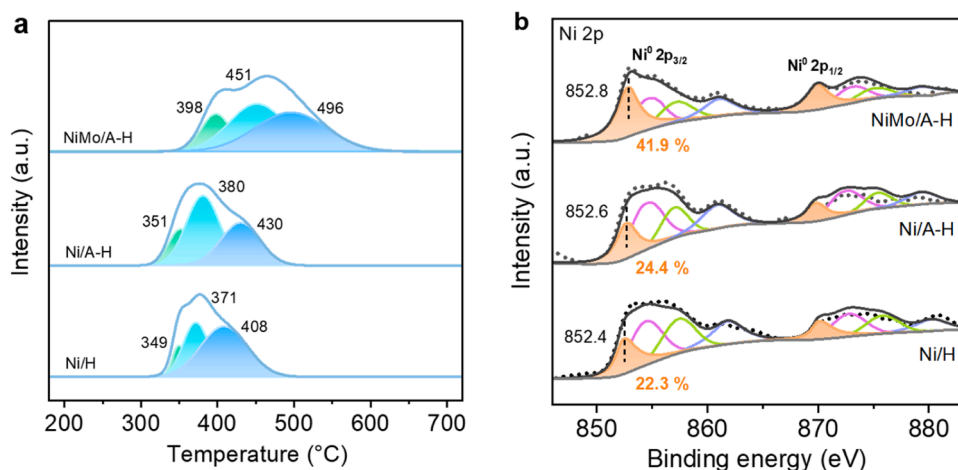


Fig. 4. (a) H₂-TPR profiles and (b) Ni 2p XPS spectra of reduced catalysts.

Table 1

Properties of various catalysts.

Catalyst	ICP-OES [%]		Metal dispersion ^a [%]	H ₂ consumption [mmolH ₂ /g _{cat}]	Particle size ^b [nm]		TOF ^c [s ⁻¹]		I _D /I _G spent
	Ni	Mo			Fresh	Spent	CH ₄	CO ₂	
Ni/H	6.1	-	12.1	0.58	19.7	23.6	0.73	0.77	0.57
Ni/A-H	6.0	-	13.8	0.59	14.7	22.1	0.84	0.86	0.64
NiMo/A-H	5.8	1.9	14.3	1.01	10.1	13.2	2.20	2.63	0.70

^a Ni dispersion was measured by CO pulse chemisorption.

^b Calculated based on TEM images.

^c Reaction condition: 50 mg catalyst, 700 °C, CH₄/CO₂ = 1/1, and GHSV 300,000 mL·g⁻¹·h⁻¹.

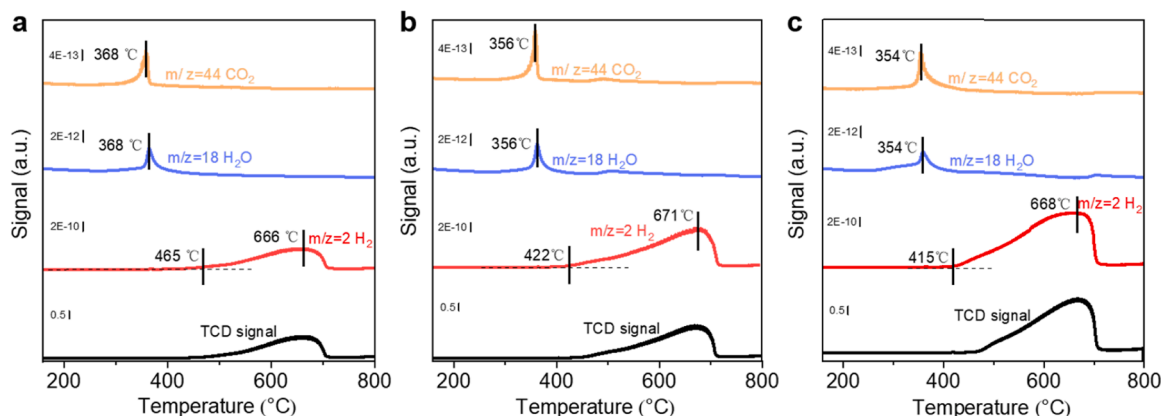


Fig. 5. CH₄-TPSR-MS of (a) Ni/H, (b) Ni/A-H, (c) NiMo/A-H catalysts.

A-H and NiMo/A-H catalysts, while it is relatively weak over Ni/H. CO₂ is typically activated on metallic Ni to produce CO [49]. A strong CO signal peak indicates that the chemisorption of CO₂ is more easily activated into CO on Ni/A-H and NiMo/A-H catalysts than on Ni/H catalysts. However, the CO₂ desorption peak of NiMo/A-H is weak, which may be due to the addition of Mo reducing the catalyst basicity [50]. In addition, the MS curves of Ni/A-H and NiMo/A-H show a strong H₂O signal, indicating that there are more hydroxyl species on the surface of catalysts, according with the Fourier Transform Infrared Spectroscopy (FT-IR) of acid-treated support.

3.3. Catalytic performance

The catalytic activity of DRM reaction over reduced catalysts was evaluated. As depicted in Fig. 6a, b, the conversion of CH₄ and CO₂ over

catalysts increase along with the reaction temperature. At various reaction temperatures ranging from 600 °C to 800 °C, NiMo/A-H and Ni/A-H exhibit remarkable levels of activity, with NiMo/A-H displaying the highest activity. Comparatively, Ni/H demonstrates lower catalytic activity. Furthermore, the TOF_{CH₄} and TOF_{CO₂} of NiMo/A-H are 2.20 s⁻¹ and 2.63 s⁻¹ at 700 °C, respectively, which is the highest among these three catalysts (Table 1). Meanwhile, the CO₂ conversion of the NiMo/A-H catalyst is higher than that of CH₄ conversion, which may be caused by the reverse water-gas shift reaction (RWGS) [51].

Fig. 6c, d show the conversion of CH₄ and CO₂ over catalysts at 800 °C for 50 h. For both Ni/H and Ni/A-H, the initial conversion decreases rapidly. Over time, the activity of Ni/H stabilizes, while Ni/A-H experiences a slow decrease. This could be due to the presence of large Ni particles in the Ni/A-H catalyst tube, which block the lumen. In contrast, the NiMo/A-H catalyst displays exceptional catalytic activity.

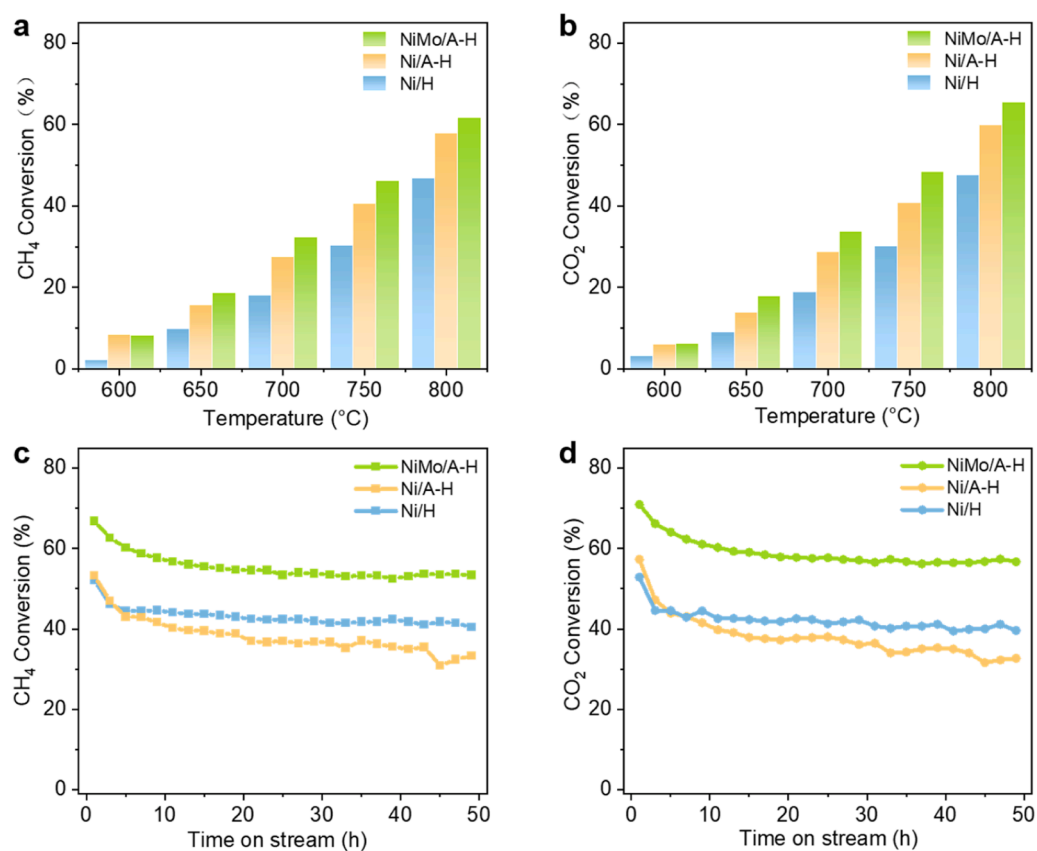


Fig. 6. (a) CH₄ and (b) CO₂ conversion of catalysts as a function of reaction temperature; (c) CH₄ and (d) CO₂ conversion of catalysts as a function of time on stream. Conditions: T = 800 °C, CH₄/CO₂ = 1/1, GHSV of 70,000 mL·g⁻¹·h⁻¹.

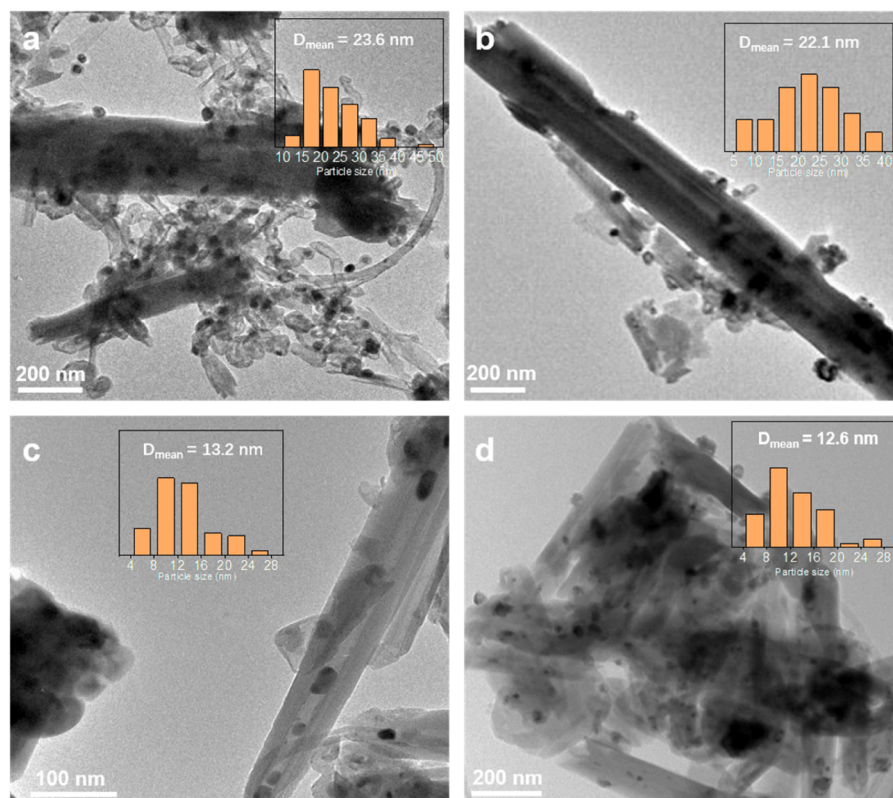


Fig. 7. TEM images of (a) Ni/H, (b) Ni/A-H, (c) NiMo/A-H spent catalysts after 50 h DRM reaction and (d) NiMo/A-H spent catalyst after 100 h DRM reaction.

The conversion of CH_4 and CO_2 over the NiMo/A-H catalyst decreases slowly at the initial stage of the reaction and stabilizes after 8 h, which is significantly higher than the previous two catalysts. In addition, to evaluate the performance of the NiMo/A-H catalyst better, its activity was tested for a longer time. The result (Fig. S11) shows that even after 100 h DRM reaction, the NiMo/A-H still maintains high and stable activity. Furthermore, the H_2/CO ratio (Fig. S12) can quantify the extent of side reactions and demonstrate the catalytic selectivity. For Ni/H and Ni/A-H catalysts, the product H_2/CO ratio is slightly higher than 1, which may be caused by the decomposition of CH_4 and the Boudouard reaction, corresponding to more carbon deposition [52]. While, the ratio of H_2/CO of NiMo/A-H is approximately equal to 1, which further proves that the NiMo/A-H catalyst is less affected by side reactions. The stability test results show that the addition of Mo to Ni-based catalysts can slightly improve the stability and maintain the high activity of the catalysts in DRM reaction.

3.4. Characterization of spent catalysts

TEM micrographs of spent catalysts after the stability test at 800°C show the sintering and carbon deposition of active components (Fig. 7). After 50 h of DRM reaction, serious metal sintering happened to the Ni/H catalyst, and the average Ni particle size was increased to 23.6 nm (Fig. 7a). Simultaneously, due to the relatively low Tammann temperature of Ni (590°C), the Ni NPs would migrate out from the HNTs during the reaction at 800°C in Ni/A-H catalysts. Consequently, the larger particle size of Ni is also observed in spent Ni/A-H catalysts (Fig. 7b). The average size of Ni particles of spent NiMo/A-H is about 13 nm (Fig. 7c), which is much smaller than that of other two spent catalysts, even after 100 h reaction (Fig. 7d). The high resistance to metal sintering is primarily due to the alloying with metals that have a high melting point, as well as the steric confinement effects. In addition,

filamentous carbon mainly grows on the surface of Ni scattered outside the HNTs. No carbon deposition is observed around the Ni particles in the lumen (Fig. S13) because the small space in the tube limits the growth of carbon. In the NiMo/A-H catalyst, the inclusion of Mo leads to a significant reduction in the quantity of carbon nanotubes. Additionally, it helps to preserve the high dispersion of Ni NPs and restricts the growth of metallic Ni grain size. According to XRD measurements (Fig. S14), spent Ni/H and Ni/A-H show more significant metal sintering. The diffraction peaks of Ni^0 in the NiMo/A-H catalyst move towards the low-angle region, indicating that Ni-Mo alloys remain intact even after long-term performance tests.

Raman spectra were performed to further investigate the properties of the carbon deposition on the spent catalysts (Fig. 8a). Two peaks were detected at approximately 1350 cm^{-1} (D-band) and 1600 cm^{-1} (G-band), which correspond to amorphous carbon and graphitic carbon, respectively [53]. The peak intensity of the D and G bands of Ni/H is the strongest, indicating that more carbon deposits are generated during the reaction, while the Ni/A-H and NiMo/A-H catalysts are less prone to coking when used extensively. The intensity ratio of the D and G bands (I_D/I_G) is calculated to track the graphitic degree of the deposited carbon, and the results are as follows: NiMo/A-H ($I_D/I_G = 0.70$) > Ni/A-H ($I_D/I_G = 0.64$) > Ni/H ($I_D/I_G = 0.57$) (Table 1). The evidence suggests that the carbon deposited on the Ni/H catalyst has a more stable structure, making it less prone to gasification. In contrast, cokes on NiMo/A-H are less graphitized and more easily to eliminate. Thermal gravimetric (TG) analysis was performed to measure the amount of carbon deposition on the surface of spent catalysts. As depicted in Fig. 8b, the weight loss of Ni/H after 50 h reaction is about 7.8 wt%, while that of Ni/A-H is 4.1 wt%. This is because some Ni particles enter the HNTs, thus generating a steric hindrance effect and inhibiting the formation of filamentous carbon. While only 2.1 wt% carbon species are formed on NiMo/A-H, and the weight loss of NiMo/A-H increases by

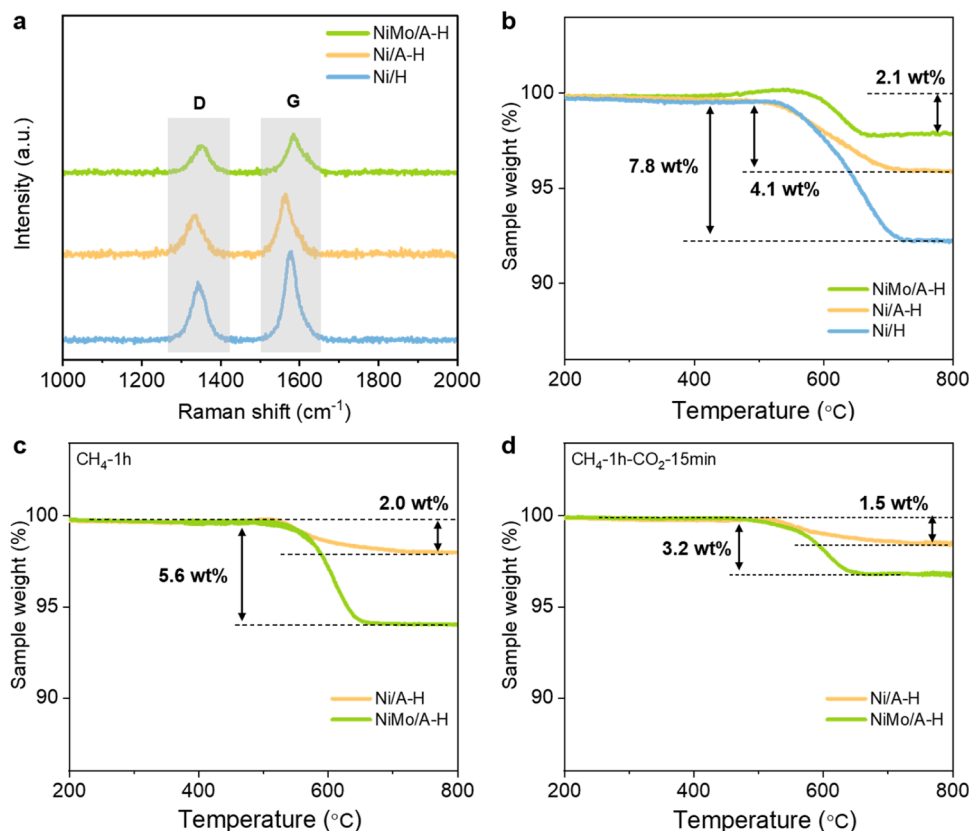


Fig. 8. (a) Raman spectra and (b) TG profiles of spent catalysts after stability test; TG profiles of the catalysts (c) after 1 h CH_4 decomposition reaction, and (d) after 1 h CH_4 decomposition reaction and 15 min flowing of CO_2 .

only 0.6 wt% (Fig. S15) even after 100 h reaction, indicating the better coking resistance. Mo species have been shown to improve the carbon resistance of Ni-based catalysts in DRM [35,36]. Furthermore, the nucleation and growth of coke can be inhibited by forming smaller Ni particle [16]. The particle size of Ni-Mo alloy is significantly smaller than that of Ni particles, as has been demonstrated previously. TG results further prove that the smaller metal particles and steric hindrance effect can enhance the coking resistance of NiMo/A-H, according with the TEM results.

Some studies have shown that the presence of Mo species can enhance the catalysts' carbon resistance in DRM. Mo doping lowers the activation energy of CH_4^* dissociation while increasing the activation energy of CH^* complete decomposition. Additionally, Mo possesses a strong attraction to O^* , and Mo doping significantly boosts the adsorption of O^* on the catalyst surface, facilitating the oxidation removal of carbon deposition [35,54,55]. To explore the carbon resistance mechanism of Mo in this study, CH_4 cracking experiments were carried out on the catalysts, and the carbon deposition was observed by TG. As shown in Fig. 8c, carbon deposition of Ni/A-H and NiMo/A-H catalysts are 2.0 and 5.6 wt% respectively after one hour of CH_4 decomposition. The NiMo/A-H catalyst produces more carbon deposition, indicating its strong ability to activate CH_4 which is consistent with results of CH_4 -TPSR above. In addition, most of the carbon species produced by NiMo/A-H catalyst is amorphous carbon which can be easily eliminated, while most of the carbon produced by Ni/A-H catalyst is graphite carbon (Fig. S16). After one hour of CH_4 reaction, CH_4 was cut off and CO_2 was injected for 15 min to observe the elimination of carbon deposits. The amount of carbon deposited on the Ni catalyst is reduced to 1.5 wt%, whereas on the NiMo/A-H catalyst it is reduced to 3.2 wt% (Fig. 8d). This suggests that NiMo/A-H catalysts have a higher rate of removing C^* , which could be attributed to their abundance of adsorbed oxygen (Fig. S17). Hence, it is reasonable to propose that the reduced carbon deposition on spent NiMo/A-H catalysts after DRM reaction is due to a balance between carbon formation and removal. In addition, a decrease in the initial activity of the catalysts in the stability test can be observed in Fig. 6. In order to explore the reason for the deactivation, the activity test of the catalysts with short time (8 h) was carried out. As shown in Fig. S18, compared with Ni/H and Ni/A-H, the activity of NiMo/A-H decreases at a slower rate with a higher conversion, which is consistent with the stability test for 50 h. According to Fig. S18c and Table S3, the inactivation of Ni/H and Ni/A-H catalysts is due to the dual action of carbon deposition and sintering, while the deactivation of NiMo/A-H is only affected by carbon deposition. At the initial stage of the reaction, NiMo/A-H produces most carbon deposition, leading to a decline in activity. Subsequently, a balance is reached between carbon formation and removal, and the conversion tends to stabilize.

3.5. Evaluation of catalyst tolerance to H_2S poisoning

The study of catalyst performance in the presence of H_2S involved the monitoring of catalyst deactivation under the exposure of 3.2 ppm H_2S , as well as the observation of activity recovery after H_2S was removed from the feed in real-time (Fig. 9). Experiments were initially performed without H_2S gas, and H_2S was introduced after 30 min. As can be seen, both catalysts display obvious deactivation after the introduction of H_2S . For Ni/A-H, the activity decreases rapidly, with CH_4 conversion dropping by 46% within one hour and almost completely deactivated after two hours exposure to H_2S (Fig. 9a). This rapid deactivation in the presence of H_2S is due to the strong chemisorption of sulfur on the Ni sites [56]. In contrast, the NiMo/A-H catalyst experiences a gradual and consistent decrease in activity with CH_4 conversion dropping by 24% within one hour. Despite being exposed to H_2S for a duration of 3 h, it still manages to maintain 19% of CH_4 conversion. The experimental results show that the stability of the catalyst is improved due to the introduction of Mo in the process of DRM with H_2S . The better H_2S resistance of the NiMo/A-H catalyst is attributed to the competitive adsorption of H_2S by Mo species, which slows down the sulfide rate of Ni. After feeding for 3 h, H_2S was stopped, and the reaction continued for 13 h without H_2S to explore the recovery of catalyst activity. It has been observed that the Ni/A-H catalyst exhibits a slight reactivation of catalytic activity (approximately 12%) after the cessation of H_2S . The high temperature of 800 °C results in a slight recovery of catalytic activity, possibly due to the desorption and oxidation of fractional sulfur adsorbed on the Ni surface [57]. However, the NiMo/A-H catalyst demonstrates a more significant recovery, with almost twice the level of activity compared to the former. Based on the results, it is found that the regeneration of NiMo/A-H is improved after discontinuing the H_2S feed as compared to the Ni catalyst. The cause of this positive occurrence is unclear, although it is believed that sulfur species tend to adhere to Mo, which quickens the release of adsorbed sulfur on the Ni surface at high temperatures. This, in turn, exposes the active site again and aids in restoring activity. Consequently, it can be seen from the above results that the addition of Mo species undoubtedly contributes to stabilizing Ni-based catalysts in the DRM process with the presence of H_2S . In addition, the H_2S resistance of catalysts with different Ni/Mo ratios was also simply studied. As shown in Fig. S19, for catalysts with Ni/Mo ratios of 5:1, 4:1, and 3:1, the resistance to H_2S enhances slightly with the increase of Mo content. However, NiMo/A-H with a Ni/Mo ratio of 4:1 has relatively better comprehensive catalytic performance in DRM. In terms of sulfur resistance alone, the optimal Ni-Mo ratio of the catalyst still needs to be further studied.

3.6. Characterization of deactivated catalysts in the presence of H_2S

XRD pattern of deactivated catalysts (Fig. S14) does not show an obvious diffraction peak of nickel or molybdenum sulfide, which may be

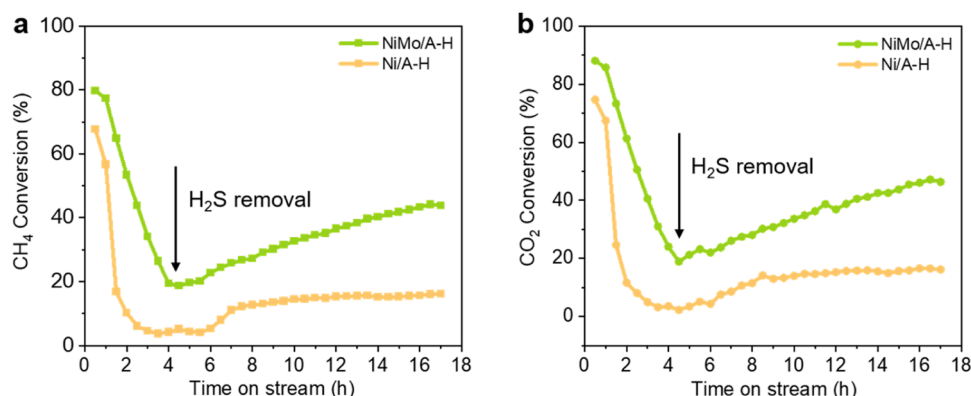


Fig. 9. (a) CH_4 and (b) CO_2 conversion of catalysts in DRM in the presence of H_2S . Conditions: Temperature = 800 °C, GHSV of 62,000 $\text{mL}\cdot\text{g}^{-1}\cdot\text{h}^{-1}$, H_2S = 3.2 ppm.

due to the poor crystallinity or small quantity [24]. Furthermore, the Ni^0 peaks of Ni/A-H and NiMo/A-H catalysts almost disappear, and the diffraction peak ascribed to the NiO crystal emerges instead, indicating that Ni^0 particles are easier to be oxidized in the H_2S -containing reaction, which is consistent with the literature reports [58]. Moreover, thermodynamic analysis shows that sulfides, especially nickel sulfides, are difficult to form when H_2S concentration is low [59]. There is also no obvious sulfide peak in the XRD pattern of sulfurized catalysts with different treatment time (Fig. S20), which proves that the sulfides are poor crystalline. The chemical states and electronic effects of Ni/A-H and NiMo/A-H catalysts during H_2S poisoning reaction were characterized by XPS (Fig. S21). It can be seen from the Ni 2p XPS spectrum that the Ni^0 peak area of sulfur poisoning catalysts decreases significantly, indicating that Ni^0 cannot be maintained well in the presence of H_2S . Meanwhile, the proportion of Ni^{2+} increases, implying that sulfur poisoning has an oxidative effect on the Ni catalyst, which is consistent with XRD results. However, the proportion of Ni^0 on NiMo/A-H (11.9%) after sulfur poisoning is significantly higher than that on Ni/A-H catalyst (4.5%), indicating the improved sulfur resistance of Mo-modified catalysts. Additionally, the valence state of Mo species in the poisoned catalyst increases overall, which may be due to the formation of high valence sulfide. These results indicate that Mo can adsorb H_2S and alleviate the poisoning of Ni^0 sites.

Surface Raman spectroscopy was further conducted to explore the changes of the surface composition of catalysts after the reaction with H_2S . In Fig. 10, it is evident that the spent Ni/A-H only has G and D band corresponding to carbon and no presence of sulfide, while the NiMo/A-H catalyst displays sulfide peaks. The peaks of NiMo/A-H at about 375 and 404 cm^{-1} belong to E_2^g and A_1^g of MoS_2 , and the three distinct peaks in the 800–1000 cm^{-1} range can be ascribed to the molecular structure of Mo_3S_{13} [60–62]. Moreover, the appearance of a small peak at 476 cm^{-1} can be attributed to the A_g phonon of NiS_2 [62,63]. This suggests that Mo species can compete to adsorb H_2S and generate sulfide authentically. The peak of MoS_x is much stronger than that of NiS_x , indicating that H_2S tends to adsorb on Mo, thus slowing down the sulphuration rate of the active Ni sites and improving the sulfur tolerance [27]. Meanwhile, D

and G peaks attributed to the carbon deposition of NiMo/A-H are small and almost negligible. Based on our observations, we believe that the absence of sulfide peaks in the Raman spectra of Ni/A-H may be due to the accumulated carbon, which covers the surface of the catalyst and makes it difficult to detect any signals of sulfide. Consequently, to eliminate the influence of carbon deposition on detection, we prepared samples that were sulfured in $\text{H}_2\text{S}/\text{N}_2$ flow with different treatment time (1, 3, 5 h). As shown in Fig. 10b, the sulfide peak is observed near 476 cm^{-1} on the Ni/A-H catalyst and increases with time. For the NiMo/A-H catalyst, the signal of molybdenum sulfide is still observed. The longer the sulfide time, the stronger the signal. All the above results show that the active metal nickel is deactivated by forming sulfide in the H_2S atmosphere, and Mo species can competitively adsorb H_2S to form sulfide, thus improving the sulfur resistance of catalysts.

Theoretical calculations based on density functional theory (DFT) were conducted to investigate the adsorption of H_2S on Ni and NiMo surfaces (Fig. 10c). The calculated adsorption energies are -0.97 , -0.94 , and -1.18 eV for H_2S adsorption on the Ni of Ni (111) surface, Ni site on NiMo (111), and Mo site on NiMo (111), respectively. It has been observed that the adsorption of H_2S on the Ni site of NiMo (111) is comparatively weaker than on the Ni site of Ni (111). Moreover, the adsorption energy is the highest at the Mo site. These simulation results suggest that H_2S tends to be adsorbed on the Mo site in NiMo alloy, indicating that Mo can play a competitive role in the adsorption of H_2S to improve the sulfur resistance of the catalyst, which is in line with the experimental results.

TG analysis of spent catalysts was performed to further investigate the effect of H_2S atmosphere on the carbon deposition of the catalyst (Fig. S22). The weight loss of the NiMo/A-H catalyst is only 1.3%, while that of the Ni/A-H catalyst is 5.5%. This indicates that the NiMo/A-H catalyst still has a good coking resistance. In other words, Mo species still play an important role in carbon deposition resistance in presence of H_2S .

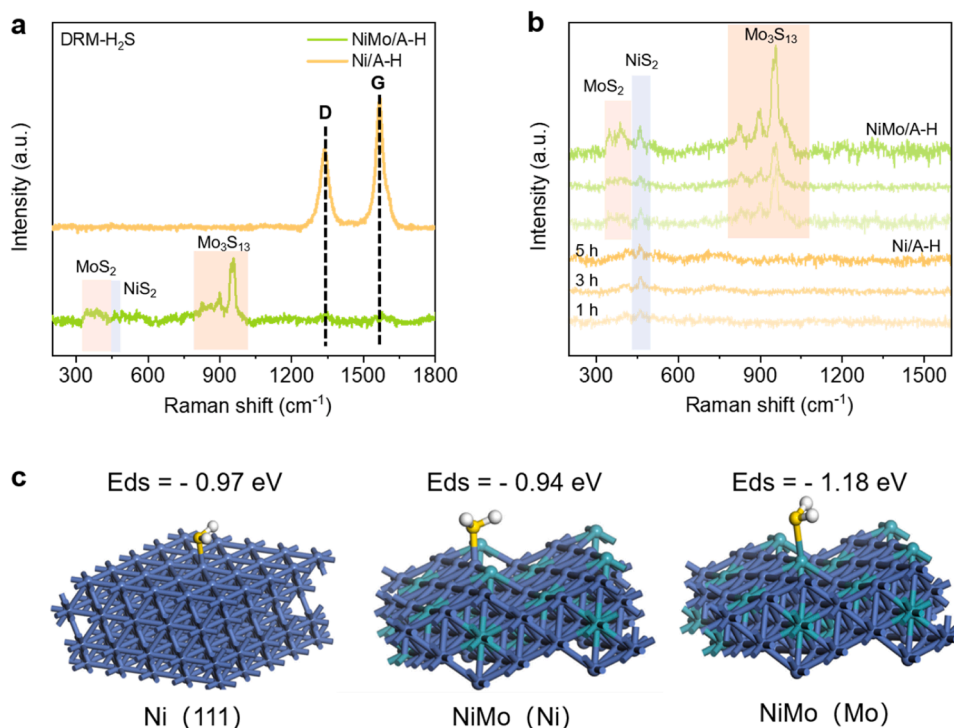


Fig. 10. Raman spectra of (a) catalysts in DRM in the presence of H_2S and (b) sulfurized catalysts with different time; (c) DFT calculation of H_2S adsorption (Ni: blue, Mo: green, S: yellow, H: white).

3.7. In situ study on DRM reaction in the presence of H_2S

The dynamic changes in the structure of Ni/A-H and NiMo/A-H catalysts under the DRM reaction with H_2S were evaluated by in situ Raman spectroscopy in different reaction atmospheres (Fig. 11). In Fig. 11a, c, the in situ Raman spectra are displayed for both catalysts under a flow of $CH_4/CO_2/N_2$ (10/10/10 mL/min) for 30 min, followed by a change to $CH_4/CO_2/H_2S$ (10/10/10 mL/min) for 90 min at 800 °C. The reaction flow is reversed in Fig. 11b, d. As shown in Fig. 11, the G band strength of Ni/A-H is much stronger than that of NiMo/A-H in the whole reaction process, which is consistent with TG results. It is noticeable that Ni/A-H exhibits a clear G band derived from deposited carbon in just 5 min while in a $CH_4/CO_2/N_2$ atmosphere (Fig. 11a). H_2S is introduced after a reaction of 30 min. Still, the intensity of the G peak of the catalyst does not change significantly, which shows that the introduction of H_2S has no significant effect on the carbon deposition produced by the catalyst. When H_2S gas is first introduced, the carbon peak may not be immediately visible. It typically takes around 10 min for the peak to become noticeable, but it becomes more prominent as time goes on (Fig. 11b). The intensity of the G-band after 30 min of reaction is lower than that shown in Fig. 11a, which indicates that H_2S influences the speed of carbon deposition. Furthermore, it is noteworthy that Fig. 11a does not display any notable sulfide peak. However, upon the initial introduction of H_2S , a faint NiS_2 peak at 480 cm^{-1} is observed in Fig. 11b. Based on the findings, it appears that the presence of H_2S in the atmosphere reduces the rate of carbon deposition on catalysts. However, this also results in the poisoning of Ni and the production of sulfide. As for the NiMo/A-H catalyst, the tendency of carbon deposition under different atmospheres is similar to that of Ni/A-H. Exposure to pure DRM gas results in rapid carbon deposition, whereas the G band appears slowly under H_2S poisoning. However, no sulfide is found on the NiMo/A-H catalyst in both cases, which may account for the low sulfide

content under high-temperature elimination. Based on the results above, it appears that H_2S influences the speed of carbon deposition, but has little effect on the amount of carbon deposition.

To acquire more reliable information during in situ reaction condition, we conducted Micro-Raman mapping at a constant 1580 cm^{-1} (Fig. S23, Fig. 12). Fig. S23a.1 is the appearance of the selected catalyst region and a.2-a.10 corresponds to the G-band intensity at each time in Fig. 11a. The intensity scale ranges from 20 to 50 for Ni/A-H, while the range of NiMo/A-H is 10–20. Compared with Fig. S23a, the G-band intensity of b.2-b.6 in Fig. S23b is much weaker affected by H_2S , corresponding to Fig. 11b. In addition, the intensity is little difference between Fig. S23a.10 and Fig. S23b.10, indicating that although Ni is poisoned by H_2S , Ni/A-H catalyst still maintains a certain balance between carbon formation and removal. Meanwhile, some interesting phenomena have been observed in the Micro-Raman mapping of NiMo/A-H (Fig. 12). Compared with Fig. 12a, the G-band intensity of NiMo/A-H in the $CH_4/CO_2/H_2S$ atmosphere (Fig. 12b) is weaker in the first 15 min. However, after 30 min of reaction, the G-band intensity increases significantly and is stronger than that of the former (Fig. 12b.6-b.10). This is different from the Ni/A-H catalyst, which might derive from the effect of Mo species. At the initial stage of the reaction, due to sulfur poisoning, the catalyst deposits less carbon. Still, as Mo gradually plays a competitive role in the adsorption of H_2S , Ni is less affected by H_2S and instead promotes the formation of carbon deposition. Hence, the intensity of the G band of the NiMo/A-H catalyst exposed to H_2S first changes uniquely from weak to strong. However, in general, the carbon deposition on NiMo/A-H is much less than that on Ni/A-H. This phenomenon suggests that Mo species still play a role in inhibiting carbon deposition, even in the presence of H_2S . The average intensity of G-band obtained in microscale are plots versus the reaction time in order to acquire the quantitative dynamics of carbon deposition (Fig. 12c, d). The introduction of H_2S would slow down the carbon deposition rate of

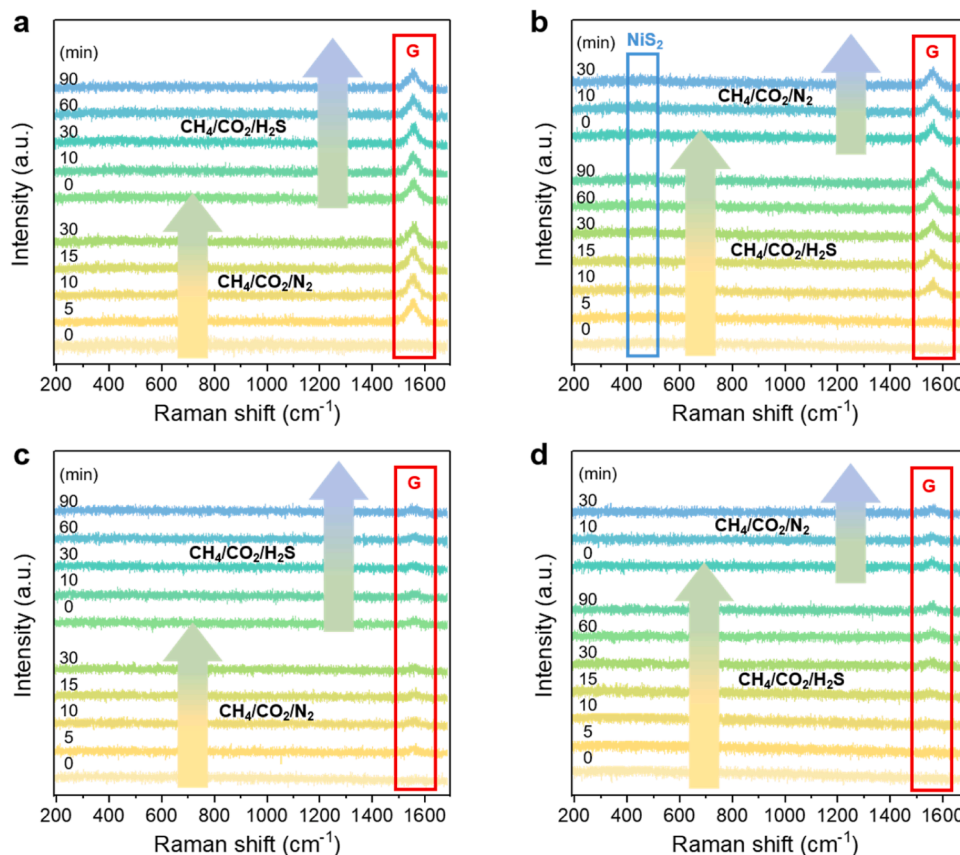


Fig. 11. In situ Raman spectra of (a, b) Ni/A-H and (c, d) NiMo/A-H catalysts in DRM in the presence of H_2S with different flow conditions.

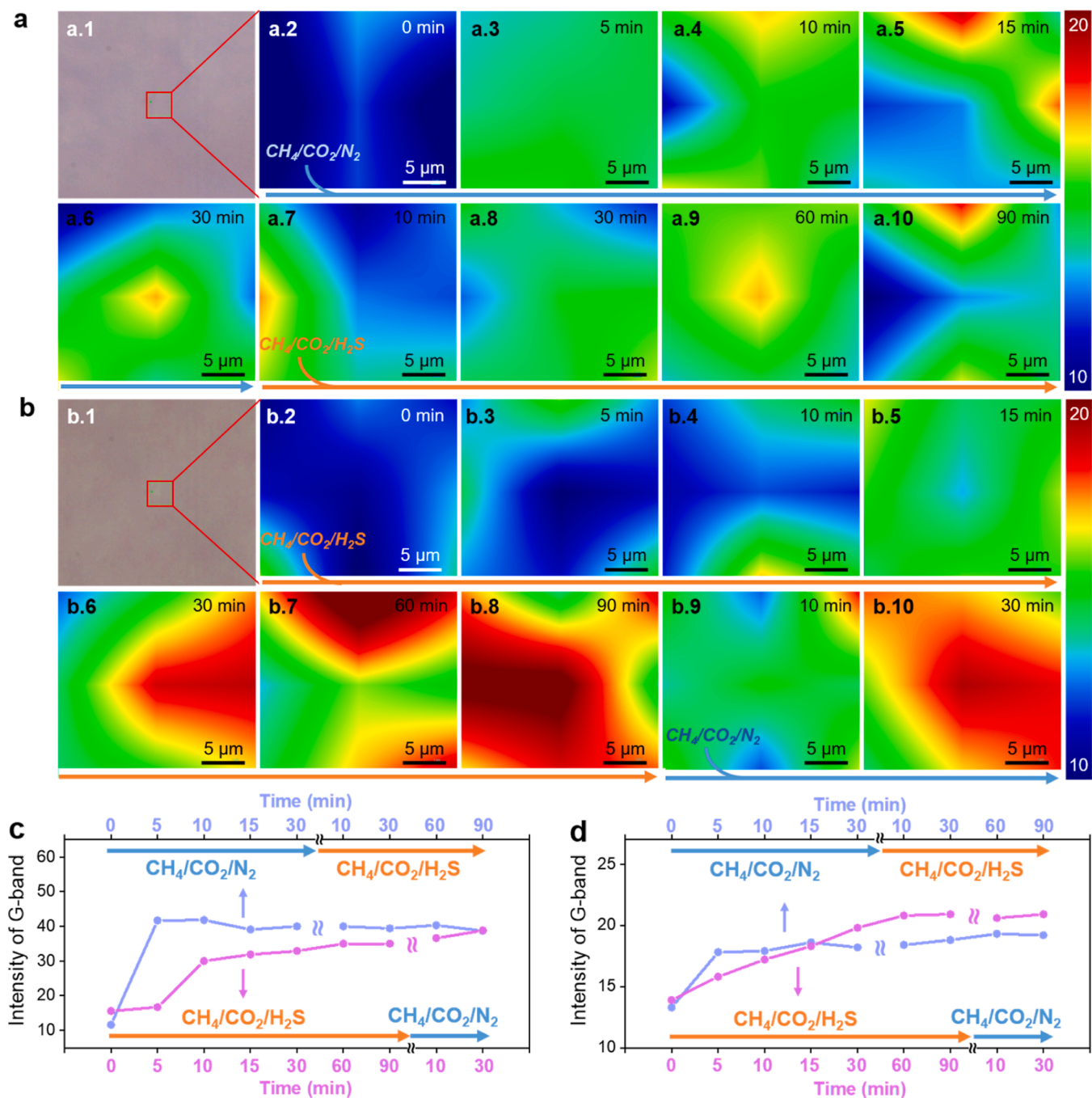


Fig. 12. Micro-Raman mapping of NiMo/A-H catalyst in DRM in the presence of H₂S with different flow conditions of (a) CH₄/CO₂/N₂ for 30 min - CH₄/CO₂/H₂S for 90 min, (b) CH₄/CO₂/H₂S for 90 min - CH₄/CO₂/N₂ for 30 min; The average intensity of G-band are plots versus the reaction time of (c) Ni/A-H, (d) NiMo/A-H catalysts.

Ni/A-H catalysts due to the decrease activation of CH₄. However, the carbon accumulation in Ni/A-H catalysts still existed. For NiMo/A-H catalysts, although, the carbon deposition rate decreases due to the poison effect of H₂S, the intensity of G-band in presence of H₂S outdoes the counterparts in absence of H₂S slightly. It further confirms the critical role of Mo on the carbon resistance.

To explore the adsorption and desorption of H₂S over Ni/A-H and NiMo/A-H catalysts, we designed the gas-flowing and static state surface reaction-mass spectra (GFSS-SR-MS) experiments (Fig. S24). The difference of the reaction gas signal and product signal between the two catalysts proves that the competitive adsorption of Mo on H₂S can slow down the Ni poisoning rate, which is consistent with the activity data.

The sulfur signal detected in the tail gas of NiMo/A-H is slightly stronger than that of Ni/A-H, indicating that sulfur species adsorbed on the NiMo/A-H catalyst are more likely to be desorbed. It may be due to the weak adsorption energy of H₂S at the Ni site on the NiMo/A-H catalyst, which corresponds to the recovery of activity after cutting off H₂S.

The schematic diagram of catalysts under different atmosphere is shown in Fig. 13. In the case of Ni/A-H, exposure to CH₄/CO₂ first leads to the preferential production of severe carbon deposition. This carbon accumulation hinders the interaction between H₂S and Ni, leading to undetectable sulfide species. Even though initial exposure to CH₄/CO₂/H₂S slows down the rate of carbon deposition in Ni/A-H catalysts, carbon accumulation still occurs on H₂S-poisoned catalysts. This suggests

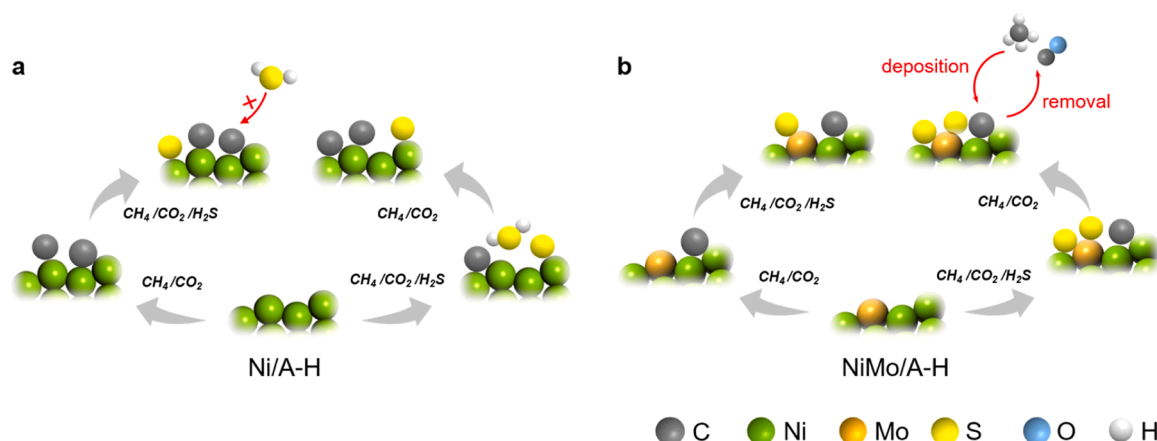


Fig. 13. Schematic illustration of reaction mechanism over (a) Ni/A-H and (b) NiMo/A-H.

that the decrease in carbon deposition rate may result from the loss of active sites, but coking still occurs due to the unchanged chemical environment. On the other hand, for NiMo/A-H catalysts, carbon deposition is inhibited under CH_4/CO_2 atmosphere. When H_2S is introduced, sulfides are formed. When NiMo/A-H catalysts are first treated with $\text{CH}_4/\text{CO}_2/\text{H}_2\text{S}$, the rate of carbon deposition also decreases. But as the reaction progresses, coking in Mo-promoted catalysts increases slightly in presence of H_2S , further confirming the critical role of Mo in coking resistance. Although H_2S adsorbed on Mo may hinder its role, the balance between carbon formation and removal remains.

4. Conclusion

In summary, the Mo modified Ni catalysts were successfully confined into halloysite nanotubes by enlarging the diameter of the lumen via selective etching by acid. The steric confinement effect limits the formation of filamentous carbon and the addition of high melting point Mo restricts the sintering of particles during the reaction. In addition, the incorporation of Mo can reduce the crystallinity of carbon deposit which is facilitative for the carbon removal. In the process of DRM, Ni-based catalysts face deactivation due to both carbon deposition and H_2S poisoning. However, the competitive adsorption of H_2S on Mo can help alleviate H_2S poisoning of Ni, which ultimately improves the sulfur resistance of the catalysts. Catalysts that solely contain Ni experience a slower initial rate of coking in the presence of H_2S due to its adsorption on Ni. In contrast, Ni catalysts enhanced by Mo experience a change in carbon deposition rate from slow to fast, but still have a lower amount of coke compared to the sole Ni catalyst. In the Mo modified Ni catalysts, Mo serves a multiple purpose. It inhibits the sintering and coking of particles, slows down the H_2S poisoning of Ni sites, and promotes the recovery of H_2S poisoned catalyst. This research establishes a connection between carbon deposition and H_2S poisoning on Ni-based catalysts. Additionally, it highlights the multiple resistance of Mo species, providing a valuable reference for the design of DRM catalysts that possess exceptional coking resistance and H_2S tolerance.

CRediT authorship contribution statement

Jiajia Zheng: Investigation, Experimental, Data analysis, Writing – original draft. **Sarawoot Impeng:** Theoretical simulation. **Jun Liu:** Data analysis, Writing – review & editing. **Jiang Deng:** Conceptualization, Investigation, Supervision, Writing – review & editing. **Dengsong Zhang:** Conceptualization, Investigation, Supervision, Writing – review & editing, Funding acquisition.

Declaration of Competing Interest

All authors declare that there are no conflicts of interest, financial or otherwise in this work; and there are no other relationships or activities that can appear to have influenced the submitted work.

Data Availability

Data will be made available on request.

Acknowledgements

The authors acknowledge the support of the National Natural Science Foundation of China (22006098, 22125604) and the Shanghai Sailing Program for Science and Technology Committee of Shanghai Municipality (20YF1413300).

Appendix A. Supporting information

Supplementary data associated with this article can be found in the online version at [doi:10.1016/j.apcatb.2023.123369](https://doi.org/10.1016/j.apcatb.2023.123369).

References

- [1] L.C. Buelens, V.V. Galvita, H. Poelman, C. Detavernier, G.B. Marin, Super-dry reforming of methane intensifies CO_2 utilization via Le Chatelier's principle, *Science* 354 (2016) 449–452.
- [2] X. Tao, M. Bai, X. Li, H. Long, S. Shang, Y. Yin, X. Dai, CH_4 - CO_2 reforming by plasma - challenges and opportunities, *Prog. Energy Combust. Sci.* 37 (2011) 113–124.
- [3] Y. Chen, J. Wei, M.S. Duyar, V.V. Ordonsky, A.Y. Khodakov, J. Liu, Carbon-based catalysts for Fischer-Tropsch synthesis, *Chem. Soc. Rev.* 50 (2021) 2337–2366.
- [4] A.L.A. Marinho, F.S. Toniolo, F.B. Noronha, F. Epron, D. Duprez, N. Bion, Highly active and stable Ni dispersed on mesoporous CeO_2 - Al_2O_3 catalysts for production of syngas by dry reforming of methane, *Appl. Catal. B: Environ.* 281 (2021), 119459.
- [5] J.J. Torrez-Herrera, S.A. Korili, A. Gil, Recent progress in the application of Ni-based catalysts for the dry reforming of methane, *Catal. Rev.* (2021) 1–58.
- [6] M. Li, A.C. van Veen, Tuning the catalytic performance of Ni-catalysed dry reforming of methane and carbon deposition via Ni-CeO_{2-x} interaction, *Appl. Catal. B: Environ.* 237 (2018) 641–648.
- [7] J. Huang, Y. Yan, S. Saqline, W. Liu, B. Liu, High performance Ni catalysts prepared by freeze drying for efficient dry reforming of methane, *Appl. Catal. B: Environ.* 275 (2020), 119109.
- [8] S.-A. Theofanidis, J.A.Z. Pieterse, H. Poelman, A. Longo, M.K. Sabbe, M. Virginie, C. Detavernier, G.B. Marin, V.V. Galvita, Effect of Rh in Ni-based catalysts on sulfur impurities during methane reforming, *Appl. Catal. B: Environ.* 267 (2020), 118691.
- [9] X. Dou, A. Veksha, W.P. Chan, W.-D. Oh, Y.N. Liang, F. Teoh, D.K.B. Mohamed, A. Giannis, G. Lisak, T.-T. Lim, Poisoning effects of H_2S and HCl on the naphthalene steam reforming and water-gas shift activities of Ni and Fe catalysts, *Fuel* 241 (2019) 1008–1018.
- [10] M. Zhang, Z. Fu, Y. Yu, Adsorption and decomposition of H_2S on the Ni(1 1 1) and Ni(2 1 1) surfaces: A first-principles density functional study, *Appl. Surf. Sci.* 473 (2019) 657–667.

- [11] V. Pawar, S. Appari, D.S. Monder, V.M. Janardhanan, Study of the combined deactivation due to sulfur poisoning and carbon deposition during biogas dry reforming on supported Ni catalyst, *Ind. Eng. Chem. Res.* 56 (2017) 8448–8455.
- [12] J. Dong, Q. Fu, H. Li, J. Xiao, B. Yang, B. Zhang, Y. Bai, T. Song, R. Zhang, L. Gao, J. Cai, H. Zhang, Z. Liu, X. Bao, Reaction-induced strong metal-support interactions between metals and inert boron nitride nanosheets, *J. Am. Chem. Soc.* 142 (2020) 17167–17174.
- [13] K. Bu, J. Deng, X. Zhang, S. Kuboon, T. Yan, H. Li, L. Shi, D. Zhang, Promotional effects of B-terminated defective edges of Ni/boron nitride catalysts for coking- and sintering-resistant dry reforming of methane, *Appl. Catal. B: Environ.* 267 (2020), 118692.
- [14] P.V. Ponugoti, P. Pathmanathan, J. Rapolu, A. Gomathi, V.M. Janardhanan, On the stability of Ni/ γ -Al₂O₃ catalyst and the effect of H₂O and O₂ during biogas reforming, *Appl. Catal. A: Gen.* 651 (2023), 119033.
- [15] C. Zhang, W. Zhu, S. Li, G. Wu, X. Ma, X. Wang, J. Gong, Sintering-resistant Ni-based reforming catalysts obtained via the nanoconfinement effect, *Chem. Commun.* 49 (2013) 9383–9385.
- [16] C. Vogt, J. Kranenborg, M. Monai, B.M. Weckhuysen, Structure sensitivity in steam and dry methane reforming over nickel: activity and carbon formation, *ACS Catal.* 10 (2019) 1428–1438.
- [17] X. Pan, X. Bao, The effects of confinement inside carbon nanotubes on catalysis, *Acc. Chem. Res.* 44 (2011) 553–562.
- [18] Y. Liu, Y. Chen, Z. Gao, X. Zhang, L. Zhang, M. Wang, B. Chen, Y. Diao, Y. Li, D. Xiao, X. Wang, D. Ma, C. Shi, Embedding high loading and uniform Ni nanoparticles into silicalite-1 zeolite for dry reforming of methane, *Appl. Catal. B: Environ.* 307 (2022), 121202.
- [19] Z. Bian, S. Das, M.H. Wai, P. Hongmanorom, S. Kawi, A review on bimetallic nickel-based catalysts for CO₂ reforming of methane, *Chemphyschem* 18 (2017) 3117–3134.
- [20] D. Zubenko, S. Singh, B.A. Rosen, Exsolution of Re-alloy catalysts with enhanced stability for methane dry reforming, *Appl. Catal. B: Environ.* 209 (2017) 711–719.
- [21] D. Liang, Y. Wang, M. Chen, X. Xie, C. Li, J. Wang, L. Yuan, Dry reforming of methane for syngas production over attapulgite-derived MFI zeolite encapsulated bimetallic Ni-Co catalysts, *Appl. Catal. B: Environ.* 322 (2023), 122088.
- [22] Q. Ma, J. Sun, X. Gao, J. Zhang, T. Zhao, Y. Yoneyama, N. Tsubaki, Ordered mesoporous alumina-supported bimetallic Pd-Ni catalysts for methane dry reforming reaction, *Catal. Sci. Tech.* 6 (2016) 6542–6550.
- [23] M. Yusuf, A.S. Farooqi, A.A. Al-Kahtani, M. Ubaidullah, M.A. Alam, L.K. Keong, K. Hellgardt, B. Abdullah, Syngas production from greenhouse gases using Ni-W bimetallic catalyst via dry methane reforming: Effect of W addition, *Int. J. Hydrog. Energy* 46 (2021) 27044–27061.
- [24] S. Das, K.H. Lim, T.Z.H. Gani, S. Aksari, S. Kawi, Bi-functional CeO₂ coated NiCo-MgAl core-shell catalyst with high activity and resistance to coke and H₂S poisoning in methane dry reforming, *Appl. Catal. B: Environ.* 323 (2023), 122141.
- [25] K. Taira, T. Sugiyama, H. Einaga, K. Nakao, K. Suzuki, Promoting effect of 2000 ppm H₂S on the dry reforming reaction of CH₄ over pure CeO₂, and in situ observation of the behavior of sulfur during the reaction, *J. Catal.* 389 (2020) 611–622.
- [26] C. Jiang, E. Loisel, D.A. Cullen, J.A. Dorman, K.M. Dooley, On the enhanced sulfur and coking tolerance of Ni-Co-rare earth oxide catalysts for the dry reforming of methane, *J. Catal.* 393 (2021) 215–229.
- [27] X. Liu, J. Yan, J. Mao, D. He, S. Yang, Y. Mei, Y. Luo, Inhibitor, co-catalyst, or intermetallic promoter? Probing the sulfur-tolerance of MoO_x surface decoration on Ni/SiO₂ during methane dry reforming, *Appl. Surf. Sci.* 548 (2021), 149231.
- [28] H. Akansu, H. Arbag, H.M. Tasdemir, S. Yasyerli, N. Yasyerli, G. Dogu, Nickel-based alumina supported catalysts for dry reforming of biogas in the absence and the presence of H₂S: Effect of manganese incorporation, *Catal. Today* 397–399 (2022) 37–49.
- [29] A. Genc, H. Arbag, H.M. Tasdemir, N. Yasyerli, S. Yasyerli, Investigation of effects of sulfur on dry reforming of biogas over nickel-iron based catalysts, *Int. J. Hydrog. Energy* (2023).
- [30] M. Massaro, C.G. Colletti, G. Lazzara, S. Milioto, R. Noto, S. Riela, Halloysite nanotubes as support for metal-based catalysts, *J. Mater. Chem. A* 5 (2017) 13276–13293.
- [31] N.M. Sanchez-Ballester, G.V. Ramesh, T. Tanabe, E. Koudelkova, J. Liu, L. K. Shrestha, Y. Lvov, J.P. Hill, K. Ariga, H. Abe, Activated interiors of clay nanotubes for agglomeration-tolerant automotive exhaust remediation, *J. Mater. Chem. A* 3 (2015) 6614–6619.
- [32] L. Deng, P. Yuan, D. Liu, P. Du, J. Zhou, Y. Wei, Y. Song, Y. Liu, Effects of calcination and acid treatment on improving benzene adsorption performance of halloysite, *Appl. Clay Sci.* 181 (2019), 105240.
- [33] Y.H. Ahmad, A.T. Mohamed, S.Y. Al-Qaradawi, Exploring halloysite nanotubes as catalyst support for methane combustion: Influence of support pretreatment, *Appl. Clay Sci.* 201 (2021), 105956.
- [34] W.-J. Li, M.-Y. Wey, Dual immobilization of PdCu nanoparticles on halloysite nanotubes by CTAB and PVP for automobile exhaust elimination, *Appl. Clay Sci.* 214 (2021), 106299.
- [35] X. Zhang, J. Deng, M. Puppevski, S. Impeng, B. Yang, G. Chen, S. Kuboon, Q. Zhong, K. Faungnawakij, L. Zheng, G. Wu, D. Zhang, High-performance binary Mo-Ni catalysts for efficient carbon removal during carbon dioxide reforming of methane, *ACS Catal.* 11 (2021) 12087–12095.
- [36] J. Tang, J. Meng, W. Pan, T. Gu, Q. Zhang, J. Zhang, X. Wang, C. Bu, G. Piao, Effect of hydroxyl and Mo doping on activity and carbon deposition resistance of hydroxyapatite supported Ni₂Mo₃ catalyst for syngas production via DRM reaction, *Int. J. Hydrog. Energy* 48 (2023) 19033–19045.
- [37] Y. Song, E. Ozdemir, S. Ramesh, A. Adishev, S. Subramanian, A. Harale, M. Albulali, B.A. Fadhel, A. Jamal, D. Moon, S.H. Choi, C.T. Yavuz, Dry reforming of methane by stable Ni-Mo nanocatalysts on single-crystalline MgO, *Science* 367 (2020) 777–781.
- [38] D. Ryaboshapka, L. Piccolo, M. Aouine, P. Bargiela, V. Briois, P. Afanasiev, Ultradispersed (Co)Mo catalysts with high hydrodesulfurization activity, *Appl. Catal. B: Environ.* 302 (2022), 120831.
- [39] Z. Yu, L.E. Fareid, K. Moljord, E.A. Blekkan, J.C. Walmsley, D. Chen, Hydrodesulfurization of thiophene on carbon nanofiber supported Co/Ni/Mo catalysts, *Appl. Catal. B: Environ.* 84 (2008) 482–489.
- [40] D. Garcia-Garcia, J.M. Ferri, L. Ripoll, M. Hidalgo, J. Lopez-Martinez, R. Balart, Characterization of selectively etched halloysite nanotubes by acid treatment, *Appl. Surf. Sci.* 422 (2017) 616–625.
- [41] G. Kresse, J. Furthmüller, Efficient iterative schemes for ab initio total-energy calculations using a plane-wave basis set, *Phys. Rev. B* 54 (1996) 11169–11186.
- [42] P.E. Blochl, Projector augmented-wave method, *Phys. Rev. B* 50 (1994) 17953–17979.
- [43] J.P. Perdew, K. Burke, M. Ernzerhof, Generalized gradient approximation made simple, *Phys. Rev. Lett.* 77 (1996) 3865–3868.
- [44] S. Grimme, J. Antony, S. Ehrlich, H. Krieg, A consistent and accurate ab initio parametrization of density functional dispersion correction (DFT-D) for the 94 elements H-Pu, *J. Chem. Phys.* 132 (2010), 154104.
- [45] H.J. Monkhorst, J.D. Pack, Special points for Brillouin-zone integrations, *Phys. Rev. B* 13 (1976) 5188–5192.
- [46] E. le Saché, L. Pastor-Pérez, D. Watson, A. Sepúlveda-Escribano, T.R. Reina, Ni stabilised in inorganic complex structures: superior catalysts for chemical CO₂ recycling via dry reforming of methane, *Appl. Catal. B: Environ.* 236 (2018) 458–465.
- [47] D. Guo, M. Li, Y. Lu, Y. Zhao, M. Li, Y. Zhao, S. Wang, X. Ma, Enhanced thermocatalytic stability by coupling nickel step sites with nitrogen heteroatoms for dry reforming of methane, *ACS Catal.* 12 (2021) 316–330.
- [48] M. Akri, S. Zhao, X. Li, K. Zang, A.F. Lee, M.A. Isaacs, W. Xi, Y. Gangarajula, J. Luo, Y. Ren, Y.T. Cui, L. Li, Y. Su, X. Pan, W. Wen, Y. Pan, K. Wilson, L. Li, B. Qiao, H. Ishii, Y.F. Liao, A. Wang, X. Wang, T. Zhang, Atomically dispersed nickel as coke-resistant active sites for methane dry reforming, *Nat. Commun.* 10 (2019) 5181.
- [49] J. Deng, M. Gao, J.-y. Hasegawa, X. Zhang, A. Wang, A. Chen, D. Zhang, Unravelling the anomalous coking resistance over boron nitride-supported Ni catalysts for dry reforming of methane, *CCS Chem.* 5 (2023) 2111–2124.
- [50] L. Yao, M.E. Galvez, C. Hu, P. Da Costa, Mo-promoted Ni/Al₂O₃ catalyst for dry reforming of methane, *Int. J. Hydrog. Energy* 42 (2017) 23500–23507.
- [51] D. Pakhare, J. Spivey, A review of dry (CO₂) reforming of methane over noble metal catalysts, *Chem. Soc. Rev.* 43 (2014) 7813–7837.
- [52] A. Tavasoli, A. Gouda, T. Zahringer, Y.F. Li, H. Quaid, C.J. Viasus Perez, R. Song, M. Sain, G. Ozin, Enhanced hybrid photocatalytic dry reforming using a phosphated Ni-CeO₂ nanorod heterostructure, *Nat. Commun.* 14 (2023) 1435.
- [53] A.C. Ferrari, J. Robertson, Interpretation of Raman spectra of disordered and amorphous carbon, *Phys. Rev. B* 61 (2000) 14095–14107.
- [54] W.-Y. Wang, J.-H. Liu, C.-Q. Lv, R.-R. Ren, G.-C. Wang, Dry reforming of methane on Ni(1 1 1) surface with different Mo doping ratio: DFT-assisted microkinetic study, *Appl. Surf. Sci.* 581 (2022), 152310.
- [55] W. Huang, C. Wei, Y. Li, Y. Zhang, W. Lin, The role of Mo species in Ni-Mo catalysts for dry reforming of methane, *Phys. Chem. Chem. Phys.* 24 (2022) 21461–21469.
- [56] X. Chen, J. Jiang, F. Yan, K. Li, S. Tian, Y. Gao, H. Zhou, Dry reforming of model biogas on a Ni/SiO₂ catalyst: overall performance and mechanisms of sulfur poisoning and regeneration, *ACS Sustain. Chem. Eng.* 5 (2017) 10248–10257.
- [57] M. Ashrafi, C. Pfeifer, T. Pröll, H. Hofbauer, Experimental study of model biogas catalytic steam reforming: 2. Impact of sulfur on the deactivation and regeneration of Ni-Based catalysts, *Energy Fuels* 22 (2008) 4190–4195.
- [58] C. Yuan, N. Yao, X. Wang, J. Wang, D. Lv, X. Li, The SiO₂ supported bimetallic Ni-Ru particles: A good sulfur-tolerant catalyst for methanation reaction, *Chem. Eng. J.* 260 (2015) 1–10.
- [59] Z. Cheng, J.-H. Wang, Y. Choi, L. Yang, M.C. Lin, M. Liu, From Ni-YSZ to sulfur-tolerant anode materials for SOFCs: electrochemical behavior, in situ characterization, modeling, and future perspectives, *Energy Environ. Sci.* 4 (2011) 4380.
- [60] J. Lin, P. Wang, H. Wang, C. Li, X. Si, J. Qi, J. Cao, Z. Zhong, W. Fei, J. Feng, Defect-rich heterogeneous MoS₂/NiS₂ nanosheets electrocatalysts for efficient overall water splitting, *Adv. Sci.* 6 (2019), 1900246.
- [61] J. Xu, G. Shao, X. Tang, F. Lv, H. Xiang, C. Jing, S. Liu, S. Dai, Y. Li, J. Luo, Z. Zhou, Frenkel-defected monolayer MoS₂ catalysts for efficient hydrogen evolution, *Nat. Commun.* 13 (2022) 2193.
- [62] S.P. Lonkar, V.V. Pillai, S.M. Alhassan, Scalable solid-state synthesis of MoS₂-NiS₂/graphene nanohybrids as bifunctional electrocatalysts for enhanced overall water splitting, *Mater. Adv.* 1 (2020) 794–803.
- [63] C. Dai, B. Li, J. Li, B. Zhao, R. Wu, H. Ma, X. Duan, Controllable synthesis of NiS and NiS₂ nanoplates by chemical vapor deposition, *Nano Res* 13 (2020) 2506–2511.